A numerical investigation of momentum flux and kinetic energy transfers between turbulent wind and propagating wave: Supplementary material

Enwei Zhang[1], Zhan Wang[*1], and Qingquan Liu[†2]

[1]Institute of Mechanics, Chinese Academy of Sciences, Beijing 100190, PR China

[2]School of Aerospace Engineering, Beijing Institute of Technology, Beijing 100081, PR China

1 Verification of the Numerical Model, Computation Domain Size, and Grid Convergence

1.1 Phase-averaging decomposition of the streamwise velocity

Figure 1 shows the triple decomposition of the instantaneous streamwise velocity for case S4. Due to the mesh motion at each time step, the phase-averaging is conducted in the following way: we output the results for each wave period (it is known that after a wave period, the grid point returns to the spatial position the same as the last wave period). This method would provide enough instantaneous results with the same wave phase and spatial position of the grid point. Then, the averaging gives the results of phase-averaged quantity. Afterward, we do the same at different phases (approximately 125 phases in this paper). Therefore, the ensemble-averaged quantity can be further obtained. Yousefi et al. (2020a) believed that the disturbance to the

[*]Corresponding author: zwang@imech.ac.cn

[†]Corresponding author: liuqq@bit.edu.cn

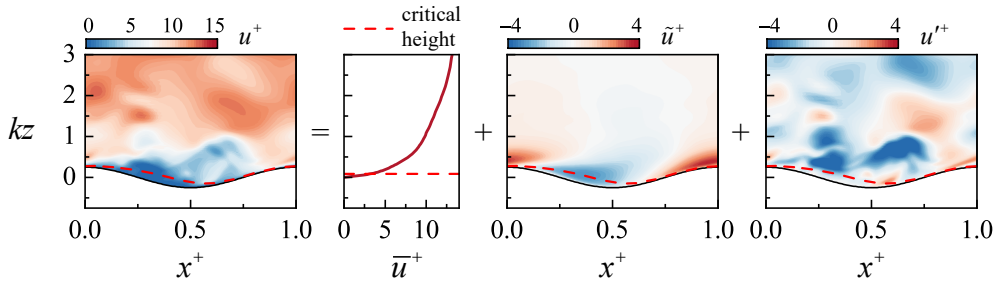

Figure 1: The phase-averaging method for decomposing the instantaneous velocity into ensemble-averaged, wave-induced, and turbulent fluctuating velocities for case S4 with $ak = 0.25$ and $c/u_\tau = 2.01$ (the streamwise coordinate is non-dimensionalized by the wavelength and the velocity is non-dimensionalized by the friction velocity). The red dashed line represents the critical height with $\langle u(z_{cl})\rangle = c$.

instantaneous flow caused by phase-averaging could be carried out using the phase of the longer peak wave. At the same time, they found that these ripples have little effect on the wavy interface by evaluating the power spectral density of the surface wave elevation. In the present study, the wave-induced quantity can be directly obtained without the effect of other ripples because there are no other components in the propagating wave.

1.2 Verification of the numerical model–additional comparison of stationary two-dimensional wavy wall and smooth wall channel flow

In the main manuscript, we verified the present numerical model through the comparison of turbulent statistics with previous experimental and numerical studies. It is seen that the velocity profile in figure 1 is very close to the numerical results by Yang and Shen (2017). However, there is a slight discrepancy between the present velocity profile and that measured by experiment (Yousefi et al., 2020a). In fact, our previous study (Zhang et al., 2021) had verified the numerical model based on the comparison of turbulent flow over stationary two-dimensional wavy wall with the experimental study by Hamed et al. (2015). It should be noted that we used the same solver and scheme while considering a LES model to accomplish the simulations. Although using a LES model, by evaluating the subgrid quantity, we found it is approximately two orders of magnitude less than the resolved quantity (Zhang et al., 2022b, 2024). In other words, the simulation reaches quasi-DNS. Therefore, we believe the present numerical model can rationally simulate the turbulent flow over wavy wall boundary and provide reliable results.

Since the smooth wall channel flow is the benchmark for various problems of wall turbulence, to make solid evidence, we also simulated smooth wall channel flow to compare the results with

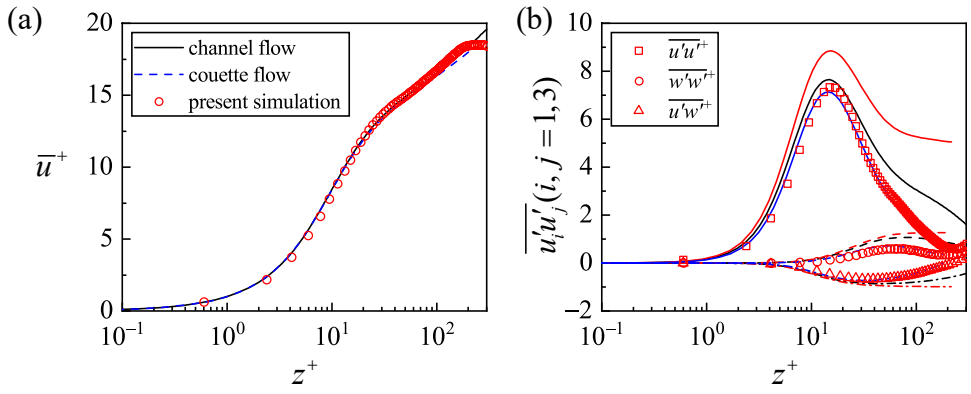

Figure 2: The comparison of (a) mean velocity profiles and (b) RMS of velocity profiles. The red symbols denote the present simulation of channel flow with $Re_\tau \approx 300$. In (a), the black solid line denotes the channel flow with $Re_\tau \approx 544$ by Lee and Moser (2015), while the blue dashed line denotes the Couette flow with $Re_\tau \approx 220$ by Lee and Moser (2018). In (b), the black line denotes the channel flow with $Re_\tau \approx 544$ by Lee and Moser (2015), the blue line denotes the channel flow with $Re_\tau \approx 180$ by Lee and Moser (2015), while the red line denotes the Couette flow with $Re_\tau \approx 220$ by Lee and Moser (2018).

that of Lee and Moser (2015). Here, the friction Reynolds number based on the half height of the channel is $Re_\tau \approx 300$. We also plot the results of Couette flow by Lee and Moser (2018). Figure 2 shows the comparison of mean velocity profiles and RMS of velocity profiles. Here, the overline denotes the time and spatial averaging, which can be regarded as a kind of ensemble-averaging. The general logarithmic law of velocity profile is captured, as shown in figure 2(a), consistent with the results by Lee and Moser (2015). Figure 2(b) shows the high-order turbulent statistics, including the streamwise Reynolds normal stress, vertical Reynolds normal stress, and Reynolds shear stress. It is found that the present simulation results fall into the region between the cases of $Re_\tau \approx 544$ and $Re_\tau \approx 180$, closer to the case of channel flow with $Re_\tau \approx 180$ by Lee and Moser (2015). Therefore, we believe the present numerical model could provide reliable data for turbulent flow over smooth or wavy boundaries.

1.3 Verification of the computation domain size

The size of the computational domain is $(x, y, z) = (2\lambda_x, \lambda_x, 0.5\lambda_x)$. A two-point spatial correlation is conducted with the time series of velocity fluctuations obtained after the turbulence is developed to ensure the domain is large enough. Figure 3 shows that the values of the correlation coefficients fall off approximately to negligibly small, which indicates enough large domain. Moreover, in our previous work on turbulent channel flow over stationary two-dimensional and

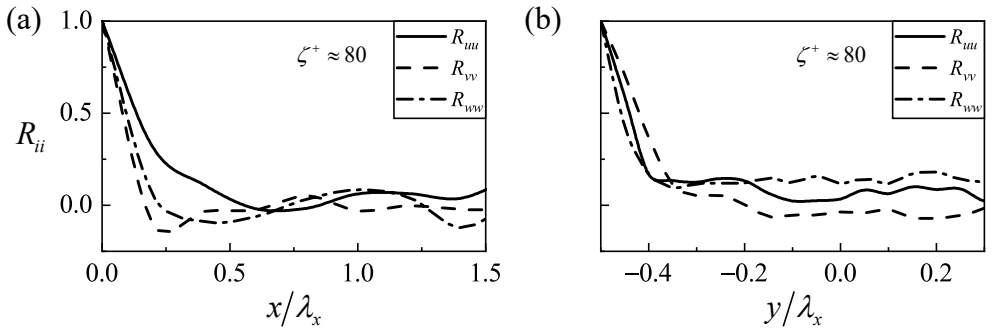

Figure 3: The two-point velocity spatial correlation coefficient at $\zeta^+ \approx 80$ along (a) streamwise and (b) spanwise directions. The solid, dashed, and dotted dashed lines denote the correlation coefficient of streamwise, spanwise, and vertical fluctuating velocities, respectively. The correlation coefficients fall negligibly small at half of the streamwise and spanwise coordinates, suggesting enough large domains.

three-dimensional wavy walls under the same Reynolds number condition (Zhang et al., 2021, 2022a,b, 2023), we set the same domain along streamwise and spanwise directions, with correlation coefficients being negligibly small (see the supplementary material in our previous study (Zhang et al., 2021)) and potentially suggesting the rational domain used in the present study. However, these studies considered stationary wavy wall turbulence, different from the current turbulent flow over moving boundaries. To make solid evidence, we enlarged the computation domain from $(x, y, z) = (2\lambda_x, \lambda_x, 0.5\lambda_x)$ (define as original domain) to $(x, y, z) = (4\lambda_x, 2\lambda_x, 0.5\lambda_x)$ (define as enlargement domain) and simulated the flow dynamics under the same condition. Figure 4 shows the comparison of turbulent statistics between these two cases, mainly around the phase-averaged streamwise velocity, turbulent kinetic energy and Reynolds shear stress. We see there is no apparent difference. The flow structures are still confined within the scale of one wavelength. Moreover, we plot the vertical profiles of these turbulent statistics, as shown in figures 4(g)(h)(i). The mean velocity, turbulent kinetic energy and Reynolds shear stress for original domain case all collapse well with that of enlargement domain case. Consequently, we believe the present computation domain size is large enough to capture the main flow structures under current conditions.

1.4 Grid convergence

Figure 5 shows the comparisons of the ensemble-averaged streamwise velocity, TKE, and RSS (normalized by the friction velocity) between cases HGR (high grid resolution) and SHGR (super high grid resolution) to verify the grid convergence. The results are shown in the wave-following curvilinear coordinate $(\xi, \zeta) = (x, \frac{z-\eta}{H})$, where η is the wave elevation and H denotes the height

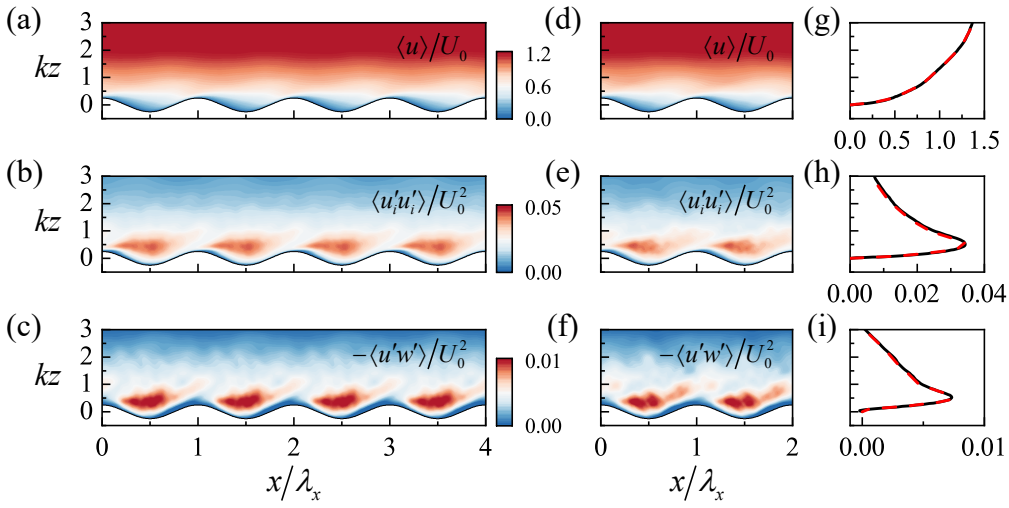

Figure 4: Comparison of turbulent statistics including phase-averaged streamwise velocity, turbulent kinetic energy, and Reynolds shear stress between enlargement domain case and original case. (a)-(c) Turbulent statistics for enlargement domain case. (d)-(f) Turbulent statistics for original domain case. (g)(h)(i) The vertical profiles of ensemble-averaged streamwise velocity, turbulent kinetic energy, and Reynolds shear stress. The black line denotes the results of enlargement domain, while red dashed line denotes the results of original domain.

of the physical domain (Yang and Shen, 2017; Cao et al., 2020). The flow was simulated through 100 periods of the propagating wave after the turbulent flow was developed, namely $100\lambda_x/c$. We also conducted averaging along the spanwise direction. Therefore, nearly 3000 samples were used for statistical analysis. It is seen that both the velocity and high-order turbulent statistics collapse well for both cases. This indicates the grid resolution for the HGR case already meets the grid-scale need.

2 Derivation of Momentum Flux and Kinetic Energy Budgets through Wave-Phase Decomposition

2.1 Transforming the momentum equations into the contributions of mean, wave-induced, and turbulent motions

The section rewrites the momentum equations using wave-phase decomposition. Firstly, substituting the velocity components based on the phase-averaging decomposition into a general

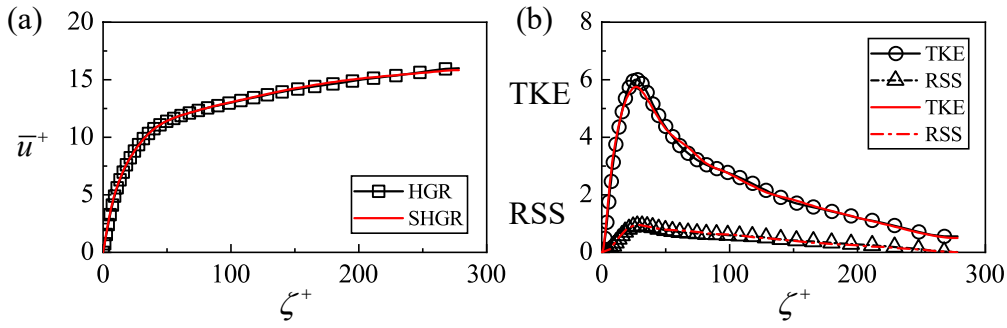

Figure 5: Grid convergence tests: comparison of the ensemble-averaged (a) streamwise velocity and (b) TKE, RSS between cases HGR and SHGR. The black lines with symbols are the results of case HGR, while the red solid and dashed lines are the results of case SHGR.

momentum conservation equation yields

$$\begin{aligned}&\frac{\partial(\overline{u}_i+\tilde{u}_i+u_i')}{\partial t}\\ &+\frac{\partial}{\partial x_j}\left(\overline{u}_i\overline{u}_j+\overline{u}_i\tilde{u}_j+\overline{u}_iu_j'+\tilde{u}_i\overline{u}_j+\tilde{u}_i\tilde{u}_j+\tilde{u}_iu_j'+u_i'\overline{u}_j+u_i'\tilde{u}_j+u_i'u_j'\right)\\ &=-\frac{1}{\rho}\frac{\partial(\overline{p}+\tilde{p}+p')}{\partial x_i}+\nu\frac{\partial^2(\overline{u}_i+\tilde{u}_i+u_i')}{\partial x_j\partial x_j}\,.\end{aligned}\tag{1}$$

After ensemble averaging, the mean momentum equations can be obtained:

$$\frac{\partial\overline{u}_i}{\partial t}+\frac{\partial}{\partial x_j}\left(\overline{u}_i\overline{u}_j+\overline{\tilde{u}_i\tilde{u}_j}+\overline{u_i'u_j'}\right)=-\frac{1}{\rho}\frac{\partial\overline{p}}{\partial x_i}+\nu\frac{\partial^2\overline{u}_i}{\partial x_j\partial x_j}\,.\tag{2}$$

The averaging meets the need of $\overline{f'}=0$, $\overline{\overline{f}}=0$, and $\overline{\tilde{f}g'}=0$. When considering the two-dimensional flow dynamics and ignoring the time-derivative term, one obtains

$$\frac{\partial}{\partial x}\left(-\overline{u}\,\overline{u}-\overline{\tilde{u}\tilde{u}}-\overline{u'u'}+\nu\frac{\partial\overline{u}}{\partial x}\right)+\frac{\partial}{\partial z}\left(-\overline{u}\,\overline{w}-\overline{\tilde{u}\tilde{w}}-\overline{u'w'}+\nu\frac{\partial\overline{u}}{\partial z}\right)=\frac{1}{\rho}\frac{\partial\overline{p}}{\partial x}\,.\tag{3}$$

Therefore, the vertical momentum flux is balanced among mean shear stress, wave-induced shear stress, Reynolds shear stress and viscous shear stress.

Another phase-averaging of equation (1) gives the phase-averaged momentum equations, expressed as

$$\begin{aligned}&\frac{\partial\overline{u}_i}{\partial t}+\frac{\partial\tilde{u}_i}{\partial t}+\frac{\partial}{\partial x_j}\left(\overline{u}_i\overline{u}_j+\overline{u}_i\tilde{u}_j+\tilde{u}_i\overline{u}_j+\tilde{u}_i\tilde{u}_j+\langle u_i'u_j'\rangle\right)\\ &\quad=-\frac{1}{\rho}\left(\frac{\partial\overline{p}}{\partial x_i}+\frac{\partial\tilde{p}}{\partial x_i}\right)+\nu\left(\frac{\partial^2\overline{u}_i}{\partial x_j\partial x_j}+\frac{\partial^2\tilde{u}_i}{\partial x_j\partial x_j}\right)\,.\end{aligned}\tag{4}$$

It is noted that $\langle\overline{f}\rangle = \overline{f}$, $\langle\tilde{f}\rangle = \tilde{f}$, and $\langle\tilde{f}\tilde{g}\rangle = \tilde{f}\tilde{g}$. The wave-induced momentum equations can be further obtained by subtracting equations (4) from (2):

$$\frac{\partial \tilde{u}_i}{\partial t} + \frac{\partial}{\partial x_j}\left(\overline{u}_i\tilde{u}_j + \tilde{u}_i\overline{u}_j + \tilde{u}_i\tilde{u}_j + \langle u_i'u_j'\rangle - \overline{\tilde{u}_i\tilde{u}_j} - \overline{u_i'u_j'}\right) = -\frac{1}{\rho}\frac{\partial \tilde{p}}{\partial x_i} + \nu\frac{\partial^2 \tilde{u}_i}{\partial x_j \partial x_j}\,. \tag{5}$$

The turbulent momentum equations can be obtained by subtracting equations (2) and (5) from (1):

$$\frac{\partial u_i'}{\partial t} + \frac{\partial}{\partial x_j}\left(u_i'\overline{u}_j + u_i'\tilde{u}_j + \overline{u}_i u_j' + \tilde{u}_i u_j' + u_i'u_j' - \langle u_i'u_j'\rangle\right) = -\frac{1}{\rho}\frac{\partial p'}{\partial x_i} + \nu\frac{\partial^2 u_i'}{\partial x_j \partial x_j}\,. \tag{6}$$

Therefore, through wave-phase decomposition, the momentum equations are transformed into three self-contained equations characterized as mean, wave-induced, and turbulent motions.

2.2 Budget equation of kinetic energy components

In wind-wave boundary layer flows, the kinetic energy transfer is related to all components' momentum equations. We further obtain the budget equations of all kinetic energy components. Firstly, rewriting equation (4) as the form of phase-averaged quantities yields

$$\frac{\partial \langle u_i\rangle}{\partial t} + \frac{\partial}{\partial x_j}\left(\langle u_i\rangle\langle u_j\rangle + \langle u_i'u_j'\rangle\right) = -\frac{1}{\rho}\frac{\partial \langle p\rangle}{\partial x_i} + \nu\frac{\partial^2 \langle u_i\rangle}{\partial x_j \partial x_j}\,. \tag{7}$$

Multiplying equation (7) with the phase-averaged velocity $\langle u_i\rangle$ would give the budget equation of phase-averaged kinetic energy:

$$\langle u_i\rangle\frac{\partial \langle u_i\rangle}{\partial t} = \langle u_i\rangle\frac{\partial}{\partial x_j}\left(-\langle u_i\rangle\langle u_j\rangle - \langle u_i'u_j'\rangle\right) - \frac{1}{\rho}\frac{\partial \langle p\rangle}{\partial x_i}\langle u_i\rangle + \nu\frac{\partial^2 \langle u_i\rangle}{\partial x_j \partial x_j}\langle u_i\rangle\,. \tag{8}$$

Equation (8) can be rewritten as

$$\frac{\mathrm{D}\langle K\rangle}{\mathrm{D}t} = \underbrace{\frac{\partial}{\partial x_j}\left(-\frac{\langle p\rangle}{\rho}\langle u_j\rangle - \langle K\rangle\langle u_j\rangle - \langle u_i\rangle\langle u_i'u_j'\rangle + 2\nu\langle S_{ij}\rangle\langle u_i\rangle\right)}_{\text{transport}} \underbrace{+\langle u_i\rangle\langle u_j\rangle\langle S_{ij}\rangle + \langle u_i'u_j'\rangle\langle S_{ij}\rangle}_{\text{production}} \underbrace{-2\nu\langle S_{ij}\rangle\langle S_{ij}\rangle}_{\text{dissipation}}\,. \tag{9}$$

Here $\langle K\rangle = \frac{1}{2}\langle u_i\rangle\langle u_i\rangle$ stands for the phase-averaged kinetic energy, $\frac{\mathrm{D}}{\mathrm{D}t} = \frac{\partial}{\partial t} + (\mathbf{u}\cdot\nabla)$ is the material derivative, and S_{ij} is the strain rate tensor. The right-hand terms of equation (9) denote kinetic energy transportation, production, and dissipation through wave-coherent motion. We see that both $-\langle u_i\rangle\langle u_j\rangle\langle S_{ij}\rangle$ and $-\langle u_i'u_j'\rangle\langle S_{ij}\rangle$ determine the phase-averaged kinetic energy production. The latter represents the energy transfer between wave-coherent motion and turbulent motion, or the turbulent kinetic energy (TKE) production, while the former term $-\langle u_i\rangle\langle u_j\rangle\langle S_{ij}\rangle$ contains

the energy transfer between wave-coherent motion and wave-induced motion, namely $-\tilde{u}_i\tilde{u}_j\langle S_{ij}\rangle$ (wave-induced kinetic energy production-WKE production). Separating these two terms with wave-phase decomposition yields:

$$T_t = -\langle u_i'u_j'\rangle\langle S_{ij}\rangle = -\langle u_i'u_j'\rangle\overline{S}_{ij} - \langle u_i'u_j'\rangle\tilde{S}_{ij} = M_t + W_t\,, \tag{10}$$

$$T_w = -\tilde{u}_i\tilde{u}_j\langle S_{ij}\rangle = -\tilde{u}_i\tilde{u}_j\overline{S}_{ij} - \tilde{u}_i\tilde{u}_j\tilde{S}_{ij} = M_w + W_w\,, \tag{11}$$

where $M_t = -\langle u_i'u_j'\rangle\overline{S}_{ij}$ ($M_w = -\tilde{u}_i\tilde{u}_j\overline{S}_{ij}$) denotes the contribution of mean shear on TKE (WKE) production. W_t in equation (10) represents the net work of wave-induced velocity gradient (i.e., wave-induced strain rate) by phase-averaged turbulent stresses, which means the production or destruction of the turbulent energy by phase-averaged turbulent stresses (Hara and Belcher, 2004; Yousefi et al., 2021). This term can also be characterized as wave-turbulence exchange. W_w in equation (11) denotes the work of the wave-induced velocity gradient by wave-induced stresses, akin to energy transportation, namely the generation of wave motion by the wave-induced shear.

Then, multiplying equation (2) with ensemble-averaged velocity $\overline{u}_i$ further gives the budget equation of mean kinetic energy:

$$\overline{u}_i\frac{\partial\overline{u}_i}{\partial t} = \overline{u}_i\frac{\partial}{\partial x_j}\left(-\overline{u}_i\overline{u}_j - \overline{\tilde{u}_i\tilde{u}_j} - \overline{u_i'u_j'}\right) - \frac{1}{\rho}\frac{\partial\overline{p}}{\partial x_i}\overline{u}_i + \nu\frac{\partial^2\overline{u}_i}{\partial x_j\partial x_j}\overline{u}_i\,. \tag{12}$$

Therefore, the budget equation for mean kinetic energy can be rewritten as

$$\frac{\mathrm{D}\overline{K}}{\mathrm{D}t} = \underbrace{\frac{\partial}{\partial x_j}\left(-\frac{\overline{p}}{\rho}\overline{u}_j - \overline{u}_i\overline{\tilde{u}_i\tilde{u}_j} - \overline{u}_i\overline{u_i'u_j'} + 2\nu\overline{S}_{ij}\overline{u}_i\right)}_{\text{transport}} \underbrace{-\overline{M}_w - \overline{M}_t}_{\text{production}} \underbrace{-2\nu\overline{S}_{ij}\overline{S}_{ij}}_{\text{dissipation}}\,, \tag{13}$$

where $\overline{K} = \frac{1}{2}\overline{u}_i\overline{u}_i$ stands for the mean kinetic energy (hereafter abbreviated as MKE). The left side of equation (13) represents the change rate of the MKE. The sum of the right-hand terms $\overline{M}_t = -\overline{u_i'u_j'}\,\overline{S}_{ij}$ and $\overline{M}_w = -\overline{\tilde{u}_i\tilde{u}_j}\,\overline{S}_{ij}$ suggests the MKE production, which denotes both turbulent stresses ($-\overline{u_i'u_j'}$) and wave-induced stresses ($-\overline{\tilde{u}_i\tilde{u}_j}$) contributing to the MKE production through their work on the mean shear, namely the sum of mean shear-induced TKE and WKE productions. The right-hand terms in the brackets describe the MKE transport via pressure, mean stress, wave-induced stress, turbulent stress, and viscous stress.

Similarly, multiplying wave-induced velocity $\tilde{u}_i$ by equation (5) and multiplying fluctuating velocity u_i' by equation (6) would yield the budget equation of wave-induced and turbulent fluctuating kinetic energies:

$$\begin{aligned}\tilde{u}_i\frac{\partial\tilde{u}_i}{\partial t} = \tilde{u}_i\frac{\partial}{\partial x_j}\left(-\overline{u}_i\tilde{u}_j - \tilde{u}_i\overline{u}_j - \tilde{u}_i\tilde{u}_j - \langle u_i'u_j'\rangle + \overline{\tilde{u}_i\tilde{u}_j} + \overline{u_i'u_j'}\right)\\ -\frac{1}{\rho}\frac{\partial\tilde{p}}{\partial x_i}\tilde{u}_i + \nu\frac{\partial^2\tilde{u}_i}{\partial x_j\partial x_j}\tilde{u}_i\,,\end{aligned} \tag{14}$$

$$u_i'\frac{\partial u_i'}{\partial t} = u_i'\frac{\partial}{\partial x_j}\left(-u_i'\overline{u}_j - u_i'\tilde{u}_j - \overline{u}_i u_j' - \tilde{u}_i u_j' - u_i'u_j' + \langle u_i'u_j'\rangle\right) \\ -\frac{1}{\rho}\frac{\partial p'}{\partial x_i}u_i' + \nu\frac{\partial^2 u_i'}{\partial x_j \partial x_j}u_i' \,. \tag{15}$$

Rewriting equations (14) and (15) gives:

$$\frac{\partial \tilde{K}}{\partial t} + \overline{u}_j\frac{\partial \tilde{K}}{\partial x_j} = \frac{\partial}{\partial x_j}\left(-\frac{\tilde{p}}{\rho}\tilde{u}_j - \tilde{u}_i\tilde{u}_i\tilde{u}_j + \tilde{u}_i\overline{\tilde{u}_i\tilde{u}_j} - \tilde{u}_i\langle u_i'u_j'\rangle + \tilde{u}_i\overline{u_i'u_j'} + 2\nu\tilde{S}_{ij}\tilde{u}_i\right) \\ \underbrace{+\tilde{u}_i\tilde{u}_j\tilde{S}_{ij}}_{-W_w} - \overline{\tilde{u}_i\tilde{u}_j}\tilde{S}_{ij} \underbrace{+\langle u_i'u_j'\rangle\tilde{S}_{ij}}_{W_t} - \overline{u_i'u_j'}\tilde{S}_{ij} - \tilde{u}_i\tilde{u}_j\overline{S}_{ij} - 2\nu\tilde{S}_{ij}\tilde{S}_{ij} \tag{16}$$

and

$$\frac{\partial K'}{\partial t} + \overline{u}_j\frac{\partial K'}{\partial x_j} = \frac{\partial}{\partial x_j}\left(-\frac{p'u_j'}{\rho} - u_i'u_i'u_j' + u_i'\langle u_i'u_j'\rangle + 2\nu S_{ij}'u_i'\right) + u_i'u_j'S_{ij}' \\ -\langle u_i'u_j'\rangle S_{ij}' - u_i'\tilde{u}_j S_{ij}' - u_i'u_j'\overline{S}_{ij} - u_i'u_j'\tilde{S}_{ij} - 2\nu S_{ij}'S_{ij}' \,. \tag{17}$$

Here, $\tilde{K} = \frac{1}{2}\tilde{u}_i\tilde{u}_i$ and $K' = \frac{1}{2}u_i'u_i'$ are the wave-induced and fluctuating turbulent kinetic energies. As equation (16) shows, the conservation equation of WKE indicates that the wave-induced shear contributes to the wave-turbulence exchange ($W_t = -\langle u_i'u_j'\rangle\tilde{S}_{ij}$) and WKE transportation ($W_w = -\tilde{u}_i\tilde{u}_j\tilde{S}_{ij}$). For the kinetic energy equation of the fluctuation component, it is seen that the work done by instantaneous turbulent stresses ($-u_i'u_j'$) on the mean shear determines the fluctuating TKE production.

A further ensemble-averaging of equation (16) leads to

$$\frac{\mathrm{D}\overline{\tilde{K}}}{\mathrm{D}t} = \underbrace{\frac{\partial}{\partial x_j}\left(-\frac{\overline{\tilde{p}\tilde{u}_j}}{\rho} - \overline{\tilde{u}_i\tilde{u}_i\tilde{u}_j} - \overline{\tilde{u}_i\langle u_i'u_j'\rangle} + 2\nu\overline{\tilde{S}_{ij}\tilde{u}_i}\right) - \overline{W}_w}_{\text{transport}} \\ \underbrace{-\overline{W}_t + \overline{M}_w}_{\text{production}} \underbrace{-2\nu\overline{\tilde{S}_{ij}\tilde{S}_{ij}}}_{\text{dissipation}} \,. \tag{18}$$

The phase-averaging and then ensemble-averaging of equation (17) gives:

$$\frac{\mathrm{D}\overline{K'}}{\mathrm{D}t} = \underbrace{\frac{\partial}{\partial x_j}\left(-\frac{\overline{p'u_j'}}{\rho} - \overline{u_i'u_i'u_j'} - \frac{1}{2}\overline{\tilde{u}_j\langle u_i'u_i'\rangle} + 2\nu\overline{S_{ij}'u_i'}\right) + \overline{u_i'u_j'S_{ij}'}}_{\text{transport}} \\ \underbrace{+\overline{M}_t + \overline{W}_t}_{\text{production}} \underbrace{-2\nu\overline{S_{ij}'S_{ij}'}}_{\text{dissipation}} \,. \tag{19}$$

The MKE production is partitioned into the productions of WKE $\overline{M}_w$ and TKE $\overline{M}_t$, with a negative sign in equations (18)–(19) compared with that in equation (13). This suggests the

kinetic energy transfer among mean, wave-induced, and turbulent motions. Moreover, the energy exchange of wave-turbulence interaction is demonstrated through equations (18)–(19), with the opposite sign of W_t. It is noted that the work done by instantaneous turbulent stress on instantaneous velocity gradient ($u_i'u_j'S_{ij}'$) is equivalent to a transport term. According to the kinetic energy conservation of all components, the production terms dominate the energy transfer. Therefore, these terms should be evaluated as the main factor in energy exchanges, as discussed in the following sections.

If assuming the mean fields are statistically steady, equations (13), (18), and (19) can be written as

$$\underbrace{\frac{\partial}{\partial x_j}\left(-\frac{\overline{p}}{\rho}\overline{u}_j-\overline{u}_i\overline{\tilde{u}_i\tilde{u}_j}-\overline{u}_i\overline{u_i'u_j'}+2\nu\overline{S}_{ij}\overline{u}_i\right)}_{\overline{T}_r}-\overline{M}_w-\overline{M}_t\underbrace{-2\nu\overline{S}_{ij}\overline{S}_{ij}}_{\overline{D}_i}=0\,, \tag{20}$$

$$\underbrace{\frac{\partial}{\partial x_j}\left(-\frac{\overline{\tilde{p}\tilde{u}_j}}{\rho}-\overline{\tilde{u}_i\tilde{u}_i\tilde{u}_j}-\overline{\tilde{u}_i\langle u_i'u_j'\rangle}+2\nu\overline{\tilde{S}_{ij}\tilde{u}_i}\right)-\overline{W}_w}_{\overline{T}_{rw}}-\overline{W}_t+\overline{M}_w\underbrace{-2\nu\overline{\tilde{S}_{ij}\tilde{S}_{ij}}}_{\overline{D}_{iw}}=0\,, \tag{21}$$

and

$$\underbrace{\frac{\partial}{\partial x_j}\left(-\frac{\overline{p'u_j'}}{\rho}-\overline{u_i'u_i'u_j'}-\frac{1}{2}\overline{\tilde{u}_j\langle u_i'u_i'\rangle}+2\nu\overline{S_{ij}'u_i'}\right)+\overline{TS_t'}}_{\overline{T}_{rt}}+\overline{M}_t+\overline{W}_t\underbrace{-2\nu\overline{S_{ij}'S_{ij}'}}_{\overline{D}_{it}}=0\,. \tag{22}$$

Therefore, kinetic energy conservation is characterized by the following equations:

$$\left.\begin{aligned}&\overline{T}_r-\overline{M}_w-\overline{M}_t+\overline{D}_i=0\\&\overline{T}_{rw}-\overline{W}_t+\overline{M}_w+\overline{D}_{iw}=0\\&\overline{T}_{rt}+\overline{M}_t+\overline{W}_t+\overline{D}_{it}=0\end{aligned}\right\}\,, \tag{23}$$

where $\overline{T}_r=\frac{\partial}{\partial x_j}\left(-\frac{\overline{p}}{\rho}\overline{u}_j-\overline{u}_i\overline{\tilde{u}_i\tilde{u}_j}-\overline{u}_i\overline{u_i'u_j'}+2\nu\overline{S}_{ij}\overline{u}_i\right)$ and $\overline{D}_i=-2\nu\overline{S}_{ij}\overline{S}_{ij}$ are the transportation and dissipation terms of MKE budget, $\overline{T}_{rw}=\frac{\partial}{\partial x_j}\left(-\frac{\overline{\tilde{p}\tilde{u}_j}}{\rho}-\overline{\tilde{u}_i\tilde{u}_i\tilde{u}_j}-\overline{\tilde{u}_i\langle u_i'u_j'\rangle}+2\nu\overline{\tilde{S}_{ij}\tilde{u}_i}\right)-\overline{W}_w$ and $\overline{D}_{iw}=-2\nu\overline{\tilde{S}_{ij}\tilde{S}_{ij}}$ are the transportation and dissipation terms of WKE budget, and $\overline{T}_{rt}=\frac{\partial}{\partial x_j}\left(-\frac{\overline{p'u_j'}}{\rho}-\overline{u_i'u_i'u_j'}-\frac{1}{2}\overline{\tilde{u}_j\langle u_i'u_i'\rangle}+2\nu\overline{S_{ij}'u_i'}\right)+\overline{TS_t'}$ and $\overline{D}_{it}=-2\overline{S_{ij}'S_{ij}'}$ are the transportation and dissipation terms of TKE budget. Here, $\overline{TS_t'}=\overline{u_i'u_j'S_{ij}'}$ is akin to the transportation and incorporated into the transport term. According to equations (23), if $\overline{M}_w$ and $\overline{M}_t$ are positive values, there is energy transfer from MKE into WKE and TKE, while the negative values mean the other way around. Similarly, a positive $\overline{W}_t$ means the energy transfer from WKE into TKE (or wave into turbulence) with a negative value the other way around.

2.3 Reynolds shear stress budget

This section describes the budget equation of RSS; thus, only the phase-averaging conduction is considered. Similarly to section 2.2, we can obtain the transport equation of RSS

$$\frac{\mathrm{D}\langle u_i' u_j' \rangle}{\mathrm{D}t} = \underbrace{-\frac{\partial}{\partial x_k}\left(\frac{\langle p' u_i' \rangle}{\rho}\delta_{jk} + \frac{\langle p' u_j' \rangle}{\rho}\delta_{ik} + \langle u_i' u_j' u_k' \rangle - \nu\frac{\partial \langle u_i' u_j' \rangle}{\partial x_k}\right)}_{\mathcal{D}_{ij}}$$
$$\underbrace{-\langle u_i' u_k' \rangle \frac{\partial \langle u_j \rangle}{\partial x_k} - \langle u_j' u_k' \rangle \frac{\partial \langle u_i \rangle}{\partial x_k}}_{\mathcal{P}_{ij}} + \underbrace{\left\langle \frac{p'}{\rho}\left(\frac{\partial u_i'}{\partial x_j} + \frac{\partial u_j'}{\partial x_i}\right)\right\rangle}_{\mathcal{F}_{ij}} \underbrace{- 2\nu\left\langle \frac{\partial u_i'}{\partial x_k}\frac{\partial u_j'}{\partial x_k}\right\rangle}_{\varepsilon_{ij}}, \tag{24}$$

where $\frac{\mathrm{D}}{\mathrm{D}t} = \frac{\partial}{\partial t} + \langle u_k \rangle \cdot \nabla$ is the material derivative, $\mathcal{P}_{ij} = -\langle u_i' u_k' \rangle \frac{\partial \langle u_j \rangle}{\partial x_k} - \langle u_j' u_k' \rangle \frac{\partial \langle u_i \rangle}{\partial x_k}$ is the production term related to the combined effect of Reynolds stress and strain rate, $\mathcal{F}_{ij} = \left\langle \frac{p'}{\rho}\left(\frac{\partial u_i'}{\partial x_j} + \frac{\partial u_j'}{\partial x_i}\right)\right\rangle$ is the re-partition term characterized by the fluctuating pressure and strain rate, $\mathcal{D}_{ij}$ is the diffusion term, and $\varepsilon_{ij} = 2\nu\left\langle \frac{\partial u_i'}{\partial x_k}\frac{\partial u_j'}{\partial x_k}\right\rangle$ is the dissipation term.

3 Results and Discussions

3.1 Propagating wave effects on wave-induced statistics

In the wind-wave boundary layer flow, the wave motion is crucial in determining the complex momentum transfer between wind and waves, which can be characterized by the wave-induced quantities (normalized by friction velocity) (detailed definition can be found in supplementary material), as shown in figure 6. Figure 6(a) suggests that a slow wave generates negative and positive wave-induced streamwise velocities on the leeward and windward sides, corresponding to the deacceleration or acceleration due to the phase-locked separating flow or airside's narrowing cross-sections (Cao and Shen, 2021). Nevertheless, the intermediate wave limits the wave-induced streamwise velocity due to the wind-wave equilibrium (Alves et al., 2003), as shown in figure 6(b). When the wave propagates fast enough, as shown in figure 6(c), an apparent phase modulation of positive wave-induced streamwise velocity can be observed at the trough, which is out-of-phase with the surface wave, agreeing with the results of Cao and Shen (2021). Figure 6(d) shows that a slow wave confines the wave vertical motion effect to the wave surface and results in the out-of-phase upper wave-induced vertical velocity. As the wave age increases, as shown in figures 6(e)(f), this effect expands to a higher vertical position even outside the wave boundary layer (WBL).

It is seen in figure 6(g) that a slow wave produces positive (negative) wave-induced RSS on the leeward (windward) side, consistent with the findings of Buckley and Veron (2016). However,

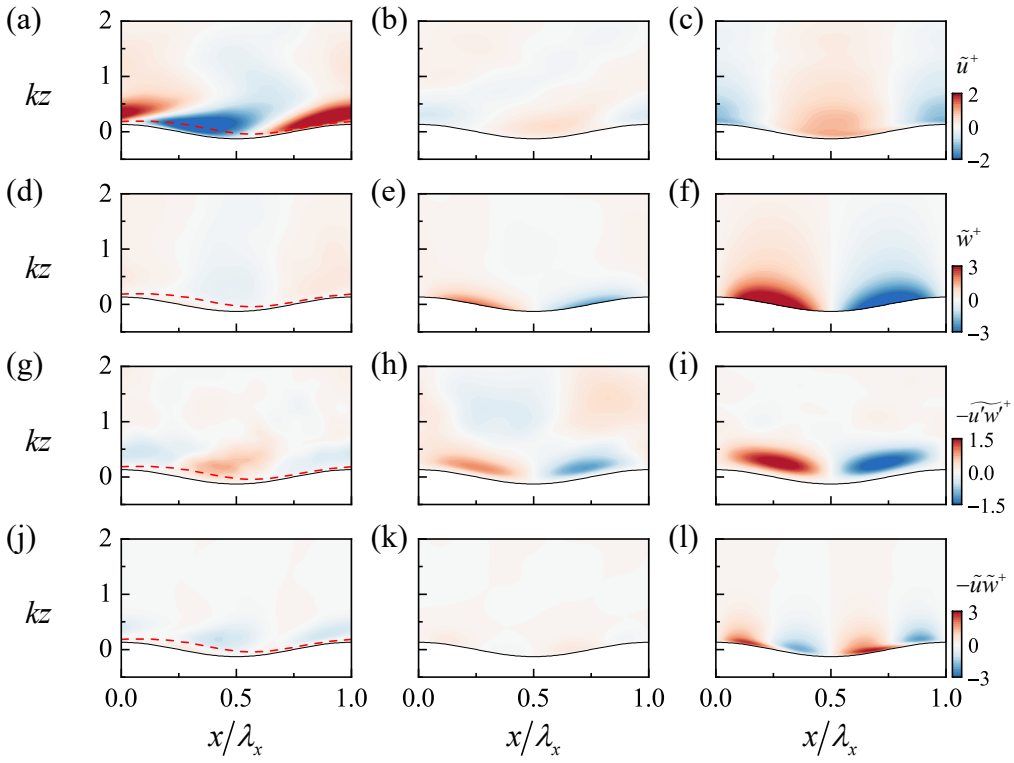

Figure 6: Contour plots of wave-induced streamwise (a-c) and vertical (d-f) velocities, wave-induced RSS (g-i), and WSS (j-l). (a)(d)(g)(j) S1 with $ak = 0.13$ and $c/u_\tau = 3.69$; (b)(e)(h)(k) I1 with $ak = 0.13$ and $c/u_\tau = 17.25$; (c)(f)(i)(l) F1 with $ak = 0.13$ and $c/u_\tau = 35.80$. The red dashed line is the critical height. All the quantities are normalized by the friction velocity.

a slight phase variation arises between positive and negative wave-induced RSS with increased wave age, as shown in figures 6(h)(i). This phenomenon has also been reported by Hsu and Hsu (1983), Kihara et al. (2007), Yousefi et al. (2020a), and Cao and Shen (2021). As a result, a symmetrically enhanced wave-induced RSS emerges.

For a slow wave, figure 6(j) indicates that the WSS near the leeward (windward) side is primarily determined by the vertical (streamwise) component of the wave-induced velocity. With the increase of wave age, the alternated positive-negative variation of WSS along waves becomes evident, as shown in figures 6(k)(l). The out-of-phase relationship between wave-induced streamwise and vertical velocities leads to an apparent $0.25\lambda_x$ phase difference between positive and negative WSS. It is worth noting that with the increases in wave age, the enhancement of WSS is confined within the region very close to the surface, which is highly related to the strengthened wave vertical motion. This corresponds to the change of WSS peak from $\zeta^+ \simeq 10$ for slow wave to $\zeta^+ \simeq 1$ for fast wave (shown in figure 3 in the main manuscript).

Figure 7 shows the ensemble-averaged RSS, WSS, and wave-induced RSS profiles (normalized

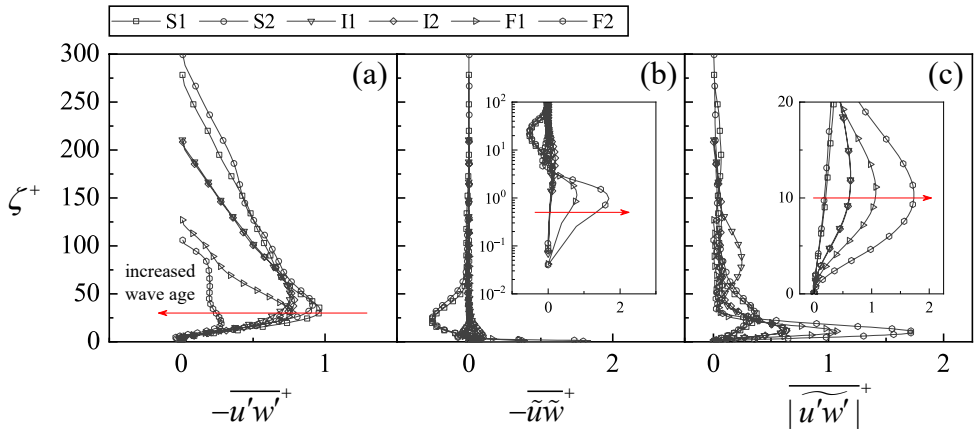

Figure 7: Vertical profiles of (a) RSS, (b) WSS, and (c) wave-induced RSS for cases S1, S2, I1, I2, F1, and F2. The red arrow indicates the trend with the rising wave age.

by u_τ^2). The decreasing trend of ensemble-averaged RSS with rising wave age in figure 7(a) suggests the possible weakening of turbulent shear by fast waves. Figure 7(b) shows a negative WSS induced by a slow wave. It indicates that a wave promotes RSS because the WSS denotes additional stress to balance the variation of turbulent stress. However, a slightly positive WSS and enhanced positive WSS can be observed in the intermediate and fast wave regimes. In particular, the enhanced WSS within the thin region ($\zeta^+ \lesssim 5$) near the surface of a fast wave denotes the suppression of RSS. We also plot the wave-induced RSS profiles by averaging the absolute value of $\widetilde{u'w'}^+$, as shown in figure 7(c). The increased wave-induced RSS for high wave age cases highlights the significance of wave-induced motion. Consequently, a fast wave suppresses the upper RSS via strong wave-induced motion.

3.2 Contour of WKE transportation

Figure 8 shows the WKE transportation, including its components that are rescaled by u_τ^4/ν. A positive (negative) value signifies an upward (downward) transport of WKE induced by wave motion. Figure 8(a) suggests that a downward (upward) WKE transport on the leeward (windward) side for a slow wave is primarily influenced by the wave-induced streamwise normal and shear stresses. While the fast wave through enhanced wave-induced vertical motion determines the WKE transport. The intermediate wave in figure 8(e) is the critical criterion starting to change the pattern of WKE transportation. It is worth noting that the governing of WKE transportation depends on the wave age, as shown in figures 8(b)-(d), 8(f)-(h), and 8(j)-(l). A slow wave determines the WKE transportation mainly by $W^+_{w,11}$, while $W^+_{w,33}$ is significant for a fast wave.

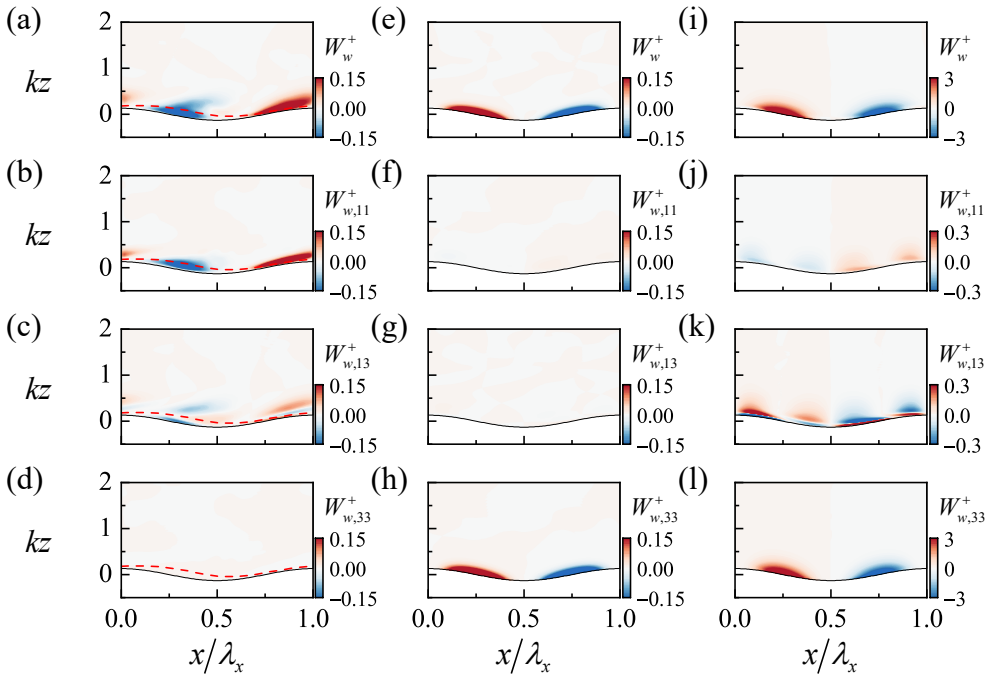

Figure 8: WKE transportation W_w^+ by wave motion. The total and components $(W_w^+, W_{w,11}^+, W_{w,13}^+, W_{w,33}^+)$ are plotted for (a-d) slow wave (S1 with $ak = 0.13$ and $c/u_\tau = 3.69$), (e-h) intermediate wave (I1 with $ak = 0.13$ and $c/u_\tau = 17.25$), and (i-l) fast wave (F1 with $ak = 0.13$ and $c/u_\tau = 35.80$). The red dashed line is the critical height.

3.3 Results of kinetic energy budgets

Figures 9(a)-(c) show the MKE budget for cases S1, I1, and F1 (normalized by the friction velocity). The mean motion consumes WKE while producing TKE for a slow wave in figure 9(a). This implies that the turbulent energy is balanced through wave motion, and the energy transportation is approximately balanced via mean dissipation. However, $\overline{M}_w^+$ no longer counteracts with $\overline{M}_t^+$ for the intermediate wave, as shown in figure 9(b), with the mean motion producing both WKE and TKE. This results in an enhanced dissipation (loss term) against production and transportation. The budget of MKE for a fast wave in figure 9(c) is the same as that of an intermediate wave but with mean energy production dominated by a higher proportion of WKE.

Figures 9(d)-(f) show the budget of WKE. For a slow wave in figure 9(d), the WKE production is balanced via energy transportation, and the wave-turbulence exchange term is smaller, which agrees with the results of Yousefi et al. (2021). Nevertheless, an intermediate wave produces WKE and transfers energy from wave to turbulence at all heights, as shown in figure 9(e). Furthermore, a fast wave in figure 9(f) amplifies the WKE production but slightly enhances wave-turbulence exchange. Thus, the fast wave motions transfer most energy into WKE. Figures 9(g)-(i) suggest

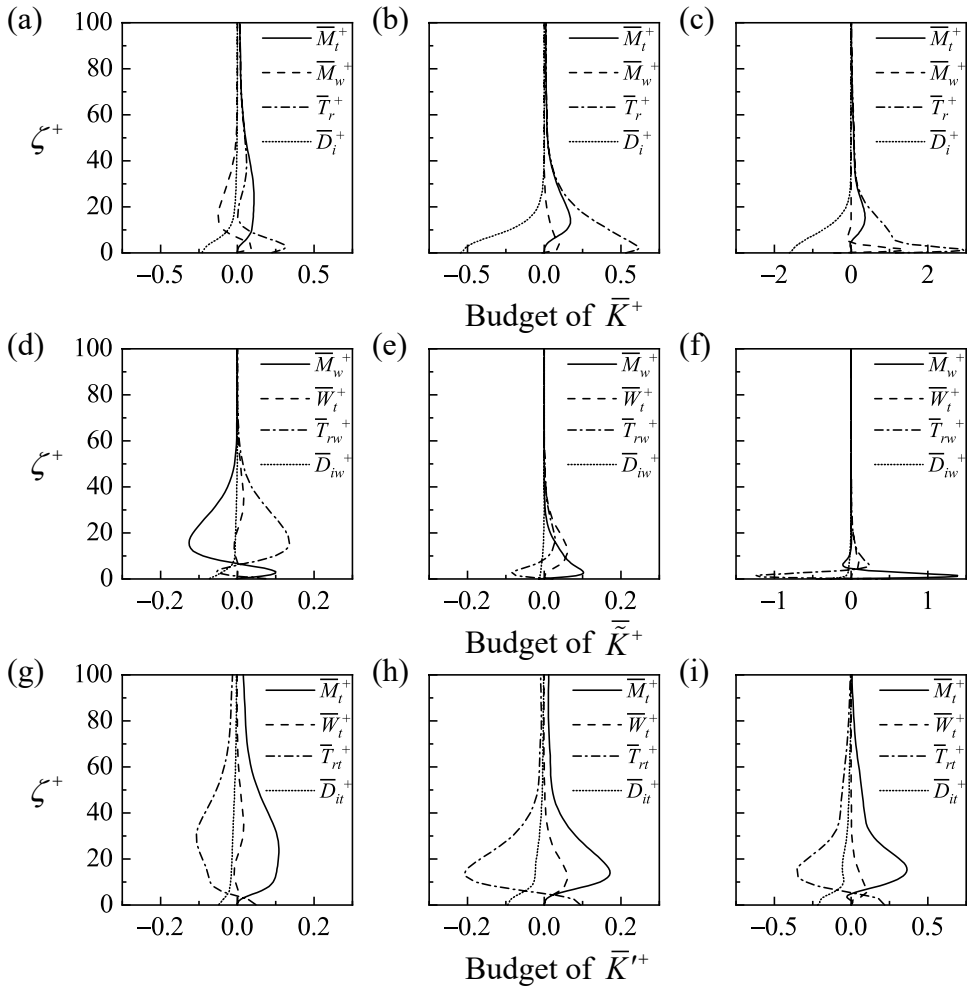

Figure 9: (a-c): budgets of MKE $\overline{K}^+$ for cases S1 ($ak = 0.13$ and $c/u_\tau = 3.69$) (a), I1 ($ak = 0.13$ and $c/u_\tau = 17.25$) (b), and F1 ($ak = 0.13$ and $c/u_\tau = 35.80$) (c). (d-f): budgets of WKE $\overline{\tilde{K}}^+$ for cases S1 (d), I1 (e), and F1 (f). (g-i): budgets of TKE $\overline{K'}^+$ for cases S1 (g), I1 (h), and F1 (i).

that the pattern of the TKE budget is approximately unaffected by wave age. $\overline{M}_t^+$ and $\overline{W}_t^+$ contribute to TKE production, and transportation and dissipation are the loss terms. However, the TKE production is strengthened with the increase of wave age, which can be attributed to the amplification of the work done by the turbulent normal stress on the mean velocity gradient.

3.4 Profiles of mean energy production terms

Figure 10 shows the profiles of $\overline{T}_t^+$ and $\overline{T}_w^+$, including the components $\overline{M}_t^+$, $\overline{W}_t^+$, $\overline{M}_w^+$, and $\overline{W}_w^+$. A slow wave-coherent flow transfers the energy into turbulence mainly via the work done by mean turbulent stresses on the mean velocity gradient, as shown in figures 10(a)-(c). In other words, the wave-turbulence exchanges can be disregarded in a slow wave. However, as the wave age

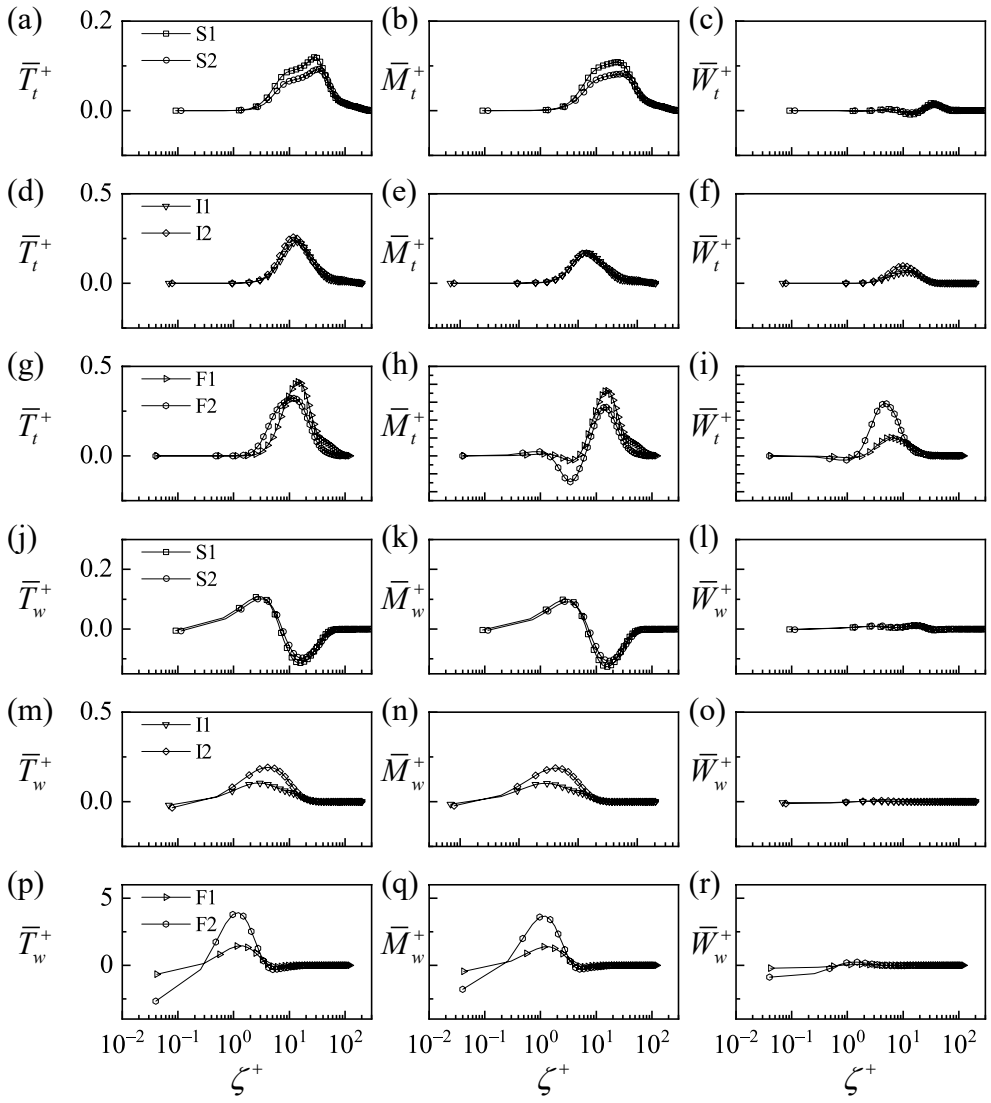

Figure 10: Profiles of $\overline{T}_t^+$, $\overline{M}_t^+$, $\overline{W}_t^+$, $\overline{T}_w^+$, $\overline{M}_w^+$, and $\overline{W}_w^+$ in a semi-logarithmic plot.

increases, wave-turbulence exchanges become more important. Figures 10(d)-(f) show that $\overline{T}_t^+$ is approximately partitioned into equal $\overline{M}_t^+$ and $\overline{W}_t^+$. A fast wave in figures 10(g)-(i) further strengthens the energy transfer into turbulence under the effect of increased mean strain rate and SRNS.

Figures 10(j)-(r) imply that the energy transfer from wave-coherent motion into wave-induced motion is mainly dominated by the work done by the wave-induced stresses on the mean strain rate. Therefore, $\overline{W}_w^+$ can be ignored (figures 10(l)(o)(r)), which agrees with Makin and Kudryavtsev (1999); Hara and Belcher (2004); Hara and Sullivan (2015); Yousefi et al. (2021). Furthermore, figure 10(j) shows that slow waves produce kinetic energy within the viscous sublayer while disrupting it in the region of $\zeta^+ > 10$. Conversely, a fast wave in figure 10(p) generates kinetic energy

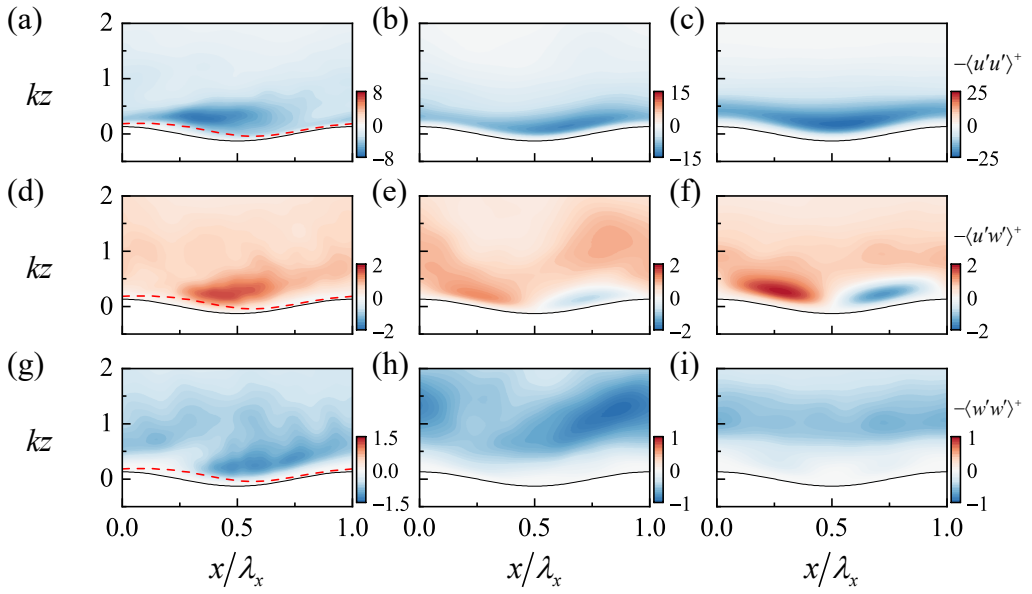

Figure 11: Contour plots of Reynolds stresses. (a)(d)(g) S1 with $ak = 0.13$ and $c/u_\tau = 3.69$; (b)(e)(h) I1 with $ak = 0.13$ and $c/u_\tau = 17.25$; (c)(f)(i) F1 with $ak = 0.13$ and $c/u_\tau = 35.80$. The red dashed line is the critical height. All the quantities are normalized by the friction velocity.

above the wind wave region. It is inferred that the $\overline{M}_w^+$ surplus (positive value) is balanced by the $\overline{M}_t^+$ deficit (negative value) within the viscous sublayer.

According to the results in figures 10(b)(e), $\overline{M}_t^+$ for slow and intermediate waves are positive. MKE thus loses energy (negative $\overline{M}_t^+$ in the MKE budget) to produce TKE (positive $\overline{M}_t^+$ in the TKE budget) through the mean strain effect. For a fast wave in figure 10(h), however, a negative $\overline{M}_t^+$ appears within the region of $\zeta^+ \leq 10$ above the wave, indicating a reverse energy transfer associated with the negative work done by the turbulent stress on the mean strain rate. Moreover, the opposite sign of $\overline{M}_w^+$ between the MKE and WKE budgets suggests energy loss or production. Figure 10(k) shows that the mean flow loses WKE within the region of $\zeta^+ \lesssim 10$ while producing WKE above this region for a slow wave. In contrast, the mean flow generates WKE in almost vertical regions when wave age increases, as shown in figures 10(n)(q).

3.5 Reynolds stress, wave-induced stress, wave-coherent velocity gradient, and wave-induced velocity gradient

In the main manuscript, we plot the turbulent kinetic energy production, wave-induced kinetic energy production, and wave-turbulence exchange. To show how the flow dynamics determine these energy transfers, we here give the results of Reynolds stress, wave-induced stress, wave-coherent velocity gradient, and wave-induced velocity gradient.

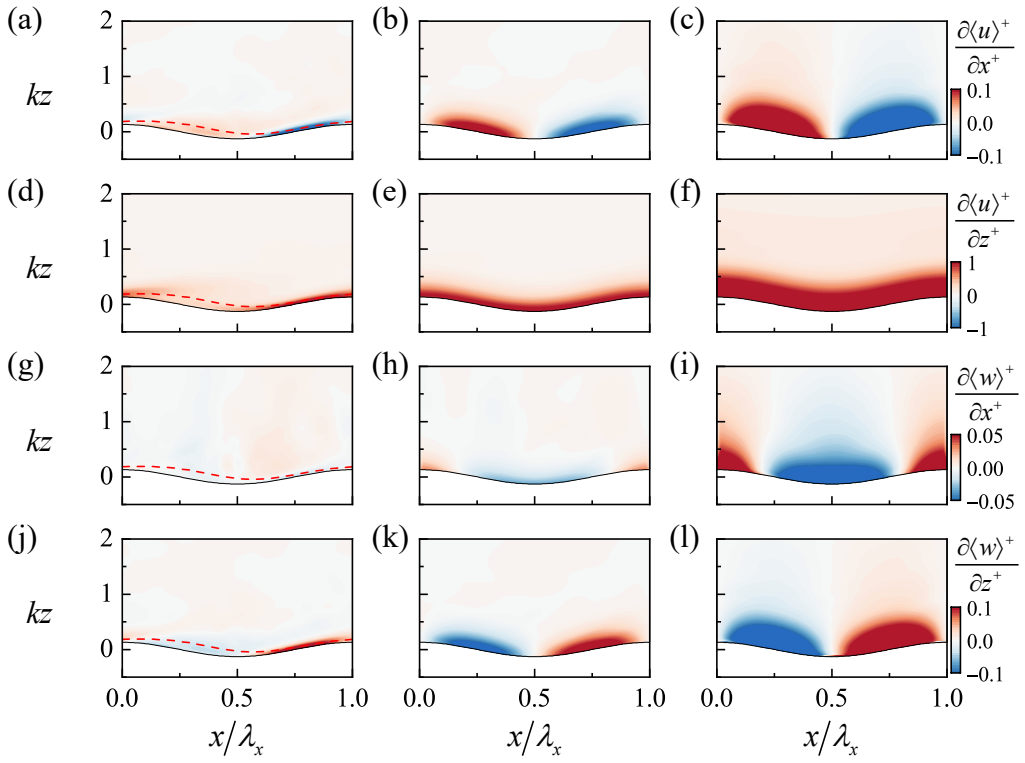

Figure 12: Contour plots of velocity gradient components. Cases same as that of figure 11.

Figure 11 show the components of Reynolds stress varying with wave age, normalized by ρu_τ^2. For streamwise Reynolds normal stress (SRNS) in figures 11(a)-(c), increasing wave age would change its spatial structure. The local enhanced SRNS appears on the leeward side (slow wave), windward side (intermediate wave), and trough (fast wave). For Reynolds shear stress (RSS) in figures 11(d)-(f), an increase in wave age results in the strengthening of negative RSS on the windward side. The positive strengthened RSS appears behind the crest (slow wave) and on the leeward side (intermediate and fast waves). For vertical Reynolds normal stress (VRNS) in figures 11(g)-(i), the rising wave age would lift the enhanced negative VRNS and be far away from the surface. Moreover, it is noted that the SRNS is approximately one order of magnitude larger than the other stresses.

Figure 12 shows the comparisons of wave-coherent velocity gradient. According to the color bar, we can see the vertical gradient of wave-coherent streamwise velocity is one order of magnitude larger than the other components. Combining the results in figures 11 and 12, the domination of $-\langle u'u'\rangle^+$ and $\frac{\partial\langle u\rangle^+}{\partial z^+}$ results in that the energy transfer between wave-coherent and turbulent motions is mainly controlled by $T^+_{t,11}$ and $T^+_{t,13}$ (as shown in figure 6 in the main manuscript).

Figure 13 shows the wave-induced stresses normalized by ρu_τ^2. It is seen that the magnitude of vertical wave-induced normal stress (VWNS) increases with wave age. Whereas streamwise

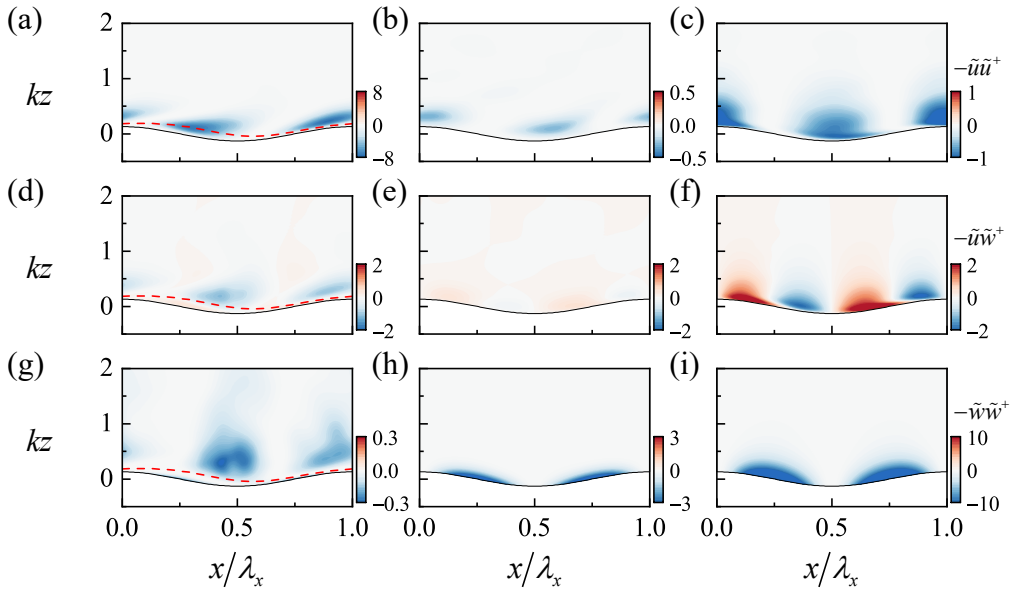

Figure 13: Contour plots of streamwise wave-induced stresses. Cases same as that of figure 11.

wave-induced normal stress (SWNS) and wave-induced shear stress (WSS) first decrease and then increase with the increases in wave age. Moreover, $-\tilde{u}\tilde{u}^+$ dominates for slow waves, while when the wave propagates fast, $-\tilde{w}\tilde{w}^+$ plays a vital role.

The energy transfer between wave-coherent and wave-induced motions is highly related to the results in figures 12 and 13. The domination of $-\tilde{w}\tilde{w}^+$ and $\frac{\partial \langle u \rangle^+}{\partial z^+}$ results in that the energy transfer is mainly controlled by $T^+_{w,11}, T^+_{w,13}$ (slow wave) and $T^+_{w,13}, T^+_{w,33}$ (intermediate and fast waves), as shown in figure 7 in the main manuscript.

Figure 14 shows the components of the wave-induced velocity gradient. The fast wave results in enhanced symmetrical $\frac{\partial \tilde{u}^+}{\partial x^+}$ and $\frac{\partial \tilde{w}^+}{\partial z^+}$. This leads to additional production terms that can be ignored under the slow wave regime. Combining the results in figures 11 and 14, the domination of $-\langle u'u' \rangle^+$ and $\frac{\partial \tilde{u}^+}{\partial x^+}, \frac{\partial \tilde{w}^+}{\partial z^+}$ causes the wave-turbulence exchange (or the energy transfer between wave-induced and turbulent motions) is mainly controlled by $W^+_{t,11}, W^+_{t,13}$ (slow wave) and $W^+_{t,11}$ (intermediate and fast waves), as shown in figure 8 in the main manuscript.

References

Alves, J.H.G., Banner, M.L., Young, I.R., 2003. Revisiting the pierson–moskowitz asymptotic limits for fully developed wind waves. Journal of Physical Oceanography 33, 1301–1323.

Buckley, M.P., Veron, F., 2016. Structure of the airflow above surface waves. J. Phys. Oceanogr. 46(5), 1377–1397.

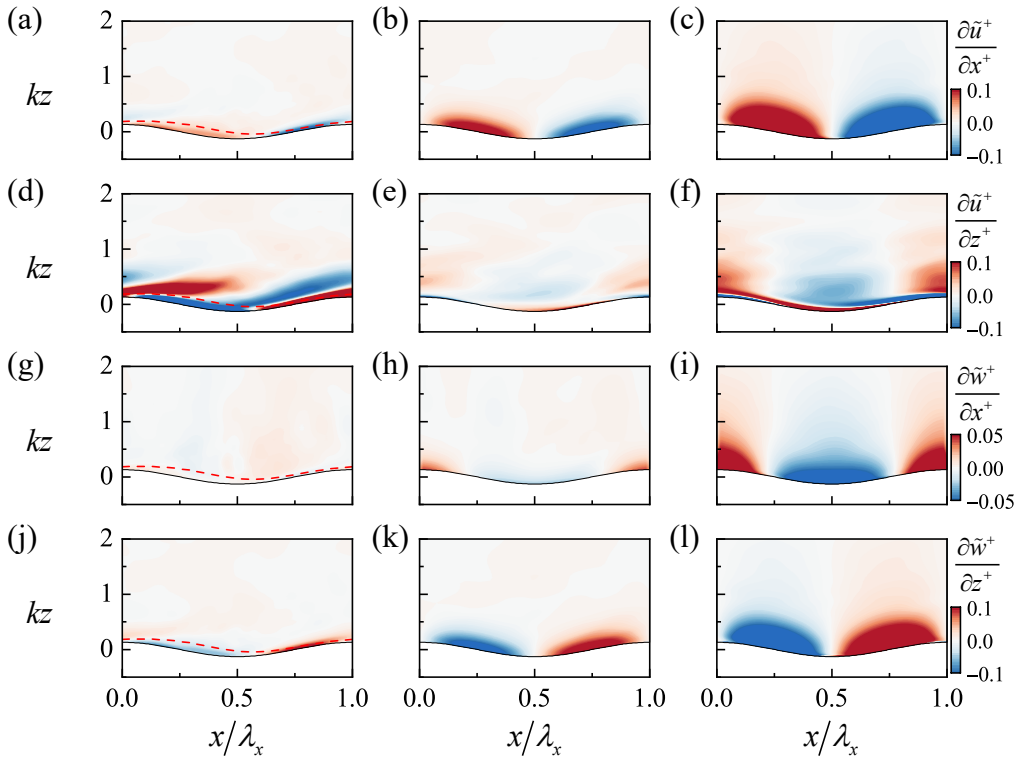

Figure 14: Contour plots of wave-induced velocity gradient components. Cases same as that of figure 11.

Cao, T., Deng, B.Q., Shen, L., 2020. A simulation-based mechanistic study of turbulent wind blowing over opposing water waves. J. Fluid Mech. 901, A27.

Cao, T., Shen, L., 2021. A numerical and theoretical study of wind over fast-propagating water waves. J. Fluid Mech. 919, A38.

Hamed, A.M., Kamdar, A., Castillo, L., Chamorro, L.P., 2015. Turbulent boundary layer over 2d and 3d large-scale wavy walls. Physics of Fluids 27, 106601.

Hara, T., Belcher, S.E., 2004. Wind profile and drag coefficient over mature ocean surface wave spectra. J. Phys. Oceanogr. 34, 2345–2358.

Hara, T., Sullivan, P.P., 2015. Wave boundary layer turbulence over surface waves in a strongly forced condition. J. Phys. Oceanogr. 45, 868–883.

Hsu, C.T., Hsu, E.Y., 1983. On the structure of turbulent flow over a progressive water wave: theory and experiment in a transformed wave-following coordinate system. part 2. Journal of Fluid Mechanics 131, 123–153.

Kihara, N., Hanazaki, H., Mizuya, T., Ueda, H., 2007. Relationship between airflow at the critical height and momentum transfer to the traveling waves. Phys. Fluids 19(1), 015102.

Lee, M., Moser, R.D., 2015. Direct numerical simulation of turbulent channel flow up to $re_\tau \approx 5200$. Journal of Fluid Mechanics 774, 395–415.

Lee, M., Moser, R.D., 2018. Extreme-scale motions in turbulent plane couette flows. Journal of Fluid Mechanics 842, 128–145.

Makin, V.K., Kudryavtsev, V.N., 1999. Coupled sea surface-atmosphere model: 1. wind over waves coupling. Journal of Geophysical Research-Oceans 104(C4), 7613–7623.

Yang, D., Shen, L., 2017. Direct numerical simulation of scalar transport in turbulent flows over progressive surface waves. J. Fluid Mech. 819, 58–103.

Yousefi, K., Veron, F., Buckley, M.P., 2020a. Momentum flux measurements in the airflow over wind-generated surface waves. J. Fluid Mech. 895, A15.

Yousefi, K., Veron, F., Buckley, M.P., 2021. Turbulent and wave kinetic energy budgets in the airflow over wind-generated surface waves. J. Fluid Mech. 920, A33.

Zhang, E.W., Wang, X.L., Liu, Q.Q., 2021. Effects of the spanwise heterogeneity of a three-dimensional wavy wall on momentum and scalar transport. Phys. Fluids 33, 055116.

Zhang, E.W., Wang, X.L., Liu, Q.Q., 2022a. Numerical investigation on the temporal and spatial statistical characteristics of turbulent mass transfer above a two-dimensional wavy wall. Int. J. Heat Mass Trans. 184, 122260.

Zhang, E.W., Wang, Z., Liu, Q.Q., 2024. Turbulent momentum and kinetic energy transfer of channel flow over three-dimensional wavy walls. Physical Review Fluids 9, 034602.

Zhang, E.W., Wang, Z., Wu, W.X., Wang, X.L., Liu, Q.Q., 2023. Secondary flow and streamwise vortices in three-dimensional staggered wavy-wall turbulence. Flow 3, E19.

Zhang, E.W., Wu, W.X., Liu, Q.Q., Wang, X.L., 2022b. Effects of vortex formation and interaction on turbulent mass transfer over a two-dimensional wavy wall. Phys. Rev. Fluids 7, 114607.